

A SYSTEMATIC SEARCH FOR DUAL AGNS IN MERGING GALAXIES (ASTRO-DARING): III: RESULTS FROM THE SDSS SPECTROSCOPIC SURVEYS

YANG-WEI ZHANG^{1,3}, YANG HUANG^{2,5}, JIN-MING BAI^{1,4,5}, XIAO-WEI LIU^{2,5}, JIAN-GUO WANG¹, XIAO-BO DONG¹

Draft version November 9, 2021

ABSTRACT

As the third installment in a series systematically searching dual active galactic nuclei (AGN) amongst merging galaxies, we present the results of 20 dual AGNs found by using the SDSS fiber spectra. To reduce the flux contamination from both the fiber aperture and seeing effects, the angular separation of two cores in our merging galaxy pairs sample is restricted at least larger than $3''$. By careful analysis of the emission lines, 20 dual AGNs are identified from 61 merging galaxies with their two cores both observed by the SDSS spectroscopic surveys. 15 of them are identified for the first time. The identification efficiency is about 32.79% (20/61), comparable to our former results (16 dual AGNs identified from 41 merging galaxies) based on the long-slit spectroscopy. Interestingly, two of the 20 dual AGNs show two prominent cores in radio images and their radio powers show they as the radio-excess AGNs. So far, 31 dual AGNs are found by our project and this is the current largest dual AGN sample, ever constructed with a consistent approach. This sample, together with more candidates from ongoing observations, is of vital importance to study the AGN physics and the coevolution between the supermassive black holes and their host galaxies.

Keywords: techniques: spectroscopic—galaxies: active – galaxies: mergers – galaxies: interactions – galaxies: nuclei

1. INTRODUCTION

Every massive galaxy is believed to host a supermassive black hole (SMBH) in the central region (e.g., Kormendy & Richstone 1995) and grows up through accretion and merger in the standard Λ cold dark matter cosmology (e.g., Kelly & Shen 2013). During the merger of two galaxies, the SMBH pairs are expected to exist and may be triggered as AGN by accreting a large number of gas into the central SMBH (e.g., Begelman et al. 1980; Hopkins et al. 2008). The kpc scale dual AGNs become natural products when the SMBH pairs are triggered as AGNs simultaneously. Moreover, dual AGNs are precursors of the pc-scale binary AGNs that will finally coalesce within Hubble time (e.g., Rodriguez et al. 2006) and could be the prominent gravitational wave signals in the Universe (e.g., Arzoumanian et al. 2016; Goulding et al. 2019).

Unlike the AGN pair (with separations greater than 15–20 kpc) representing the earliest stage of the binary SMBH evolution, the dual AGNs are much closer (with separations between few hundred pc and 10–15 kpc) and thus serve as a vital observational tool to probe the galaxy evolution and AGN physics, especially the coevolution between the central BHs and their host galaxies (e.g., Volonteri et al. 2003; Colpi and Dotti 2011; Yu et al. 2011; Kormendy & Ho 2013). However, identifying dual AGNs is not an easy task and the currently confirmed number (around 70, see a compilation in Huang et al. 2021 – hereafter Paper I; Zhang et al. 2021a – Paper II) is largely smaller than that of the theoretical prediction (e.g., Komossa & Zensus 2016). In

prior to this project, the most ambitious dual AGN systematically searching method is based on the follow-up observations of double-peaked AGNs (DPAGNs) found either from the SDSS survey (e.g., Wang et al. 2009; Liu et al. 2010a; Smith et al. 2010) or from the DEEP survey (e.g., Gerke et al. 2007; Comerford et al. 2009a). However, only 2% to 5% of those selected DPAGNs, as revealed by long-slit or integral field-unit spectroscopy follow-up observations, are confirmed as dual AGNs (e.g., Shen et al. 2011; Comerford et al. 2011, 2012; Fu et al. 2012). The double-peaked emission-line profiles are largely contributed by the complicate gas kinematics around single AGN rather than dual AGN (e.g., Shen et al. 2011; Fu et al. 2012; Nevin et al. 2016). Recently, other systematically searching methods are also proposed based on hard X-ray imaging (e.g., Komossa et al. 2003; Koss et al. 2011, 2016; Liu et al. 2013; Comerford et al. 2015), radio imaging (e.g., Fu et al. 2011b, 2015a; Müller-Sánchez et al. 2015), and infrared colors (e.g., Satyapal et al. 2014, 2017). But the number of identified dual AGNs is still quite limited.

As stated in our Paper I and II, an innovative method of systematically searching of dual AGNs in merging galaxies has been developed and 222 candidates are selected. A brief description of the candidate selection is presented in Section 2. In our Paper II, 41 of the 222 candidates have been observed by the long-slit spectroscopy using the YFOSC mounted on the Lijiang 2.4 m telescope (LJT) of Yunnan observatories. By careful analysis, 16 of the 41 observed merging galaxies are identified as dual AGN and the identification efficiency is about 40 %.

In this work, we continue our systematic searching of dual AGNs by the fiber spectra from the SDSS archived data. Doing so, 61 merging galaxies from our 222 candidates are found with both cores observed by the SDSS fiber spectra under good seeing conditions. By analysis of emission lines, 20 systems are identified as dual AGNs and the efficiency is similar to that in our Paper II, implying the success of our searching approach. The paper is structured as follows. The data

¹ Yunnan Observatories, Chinese Academy of Sciences, Kunming, Yunnan 650011, China; zhangyangwei@ynao.ac.cn; baijinming@ynao.ac.cn

² South-Western Institute for Astronomy Research, Yunnan University, Kunming 650500, China; yanghuang@ynu.edu.cn

³ University of Chinese Academy of Sciences, Beijing 100049, China

⁴ Key Laboratory for the Structure and Evolution of Celestial Objects, Chinese Academy of Sciences, Kunming 650011, China

⁵ Corresponding authors

Table 1
SDSS Observational information for the 20 dual AGNs

Name	Core	R.A.(J2000)	Decl.(J2000)	Seeing ($''$)	Separation ($''$ /kpc)	g band (mag)	Flux _{contam}	Observing date (UT)	PA ($^\circ$)
(1)	(2)	(3)	(4)	(5)	(6)	(7)	(8)	(9)	(10)
J080544.13+113040.30	J0805+1130EN	121.43468	11.51171	1.50	3.3/10.8	19.60	1.4 %	20110211	56.0
	J0805+1130WS	121.43391	11.51120	2.33		18.13	1.2 %	20060223	
J084809.69+351532.12	J0848+3515EN	132.04216	35.25953	1.47	5.7/6.3	16.16	0.0 %	20030202	67.3
	J0848+3515WS	132.04038	35.25892	1.91		16.18	0.0 %	20110312	
J090714.61+520350.61	J0907+5203EN	136.81088	52.06406	2.06	7.4/8.5	17.83	0.0 %	20010324	11.9
	J0907+5203WS	136.81020	52.06206	2.34		16.93	0.0 %	20010329	
J091448.94+085324.45	J0914+0853WN	138.70394	8.89013	1.83	3.8/9.4	18.35	0.2 %	20111230	153.4
	J0914+0853ES	138.70440	8.88920	1.58		18.83	0.1 %	20031201	
J095559.35+395438.87	J0955+3954EN	148.99952	39.91302	1.85	10.1/9.7	16.52	0.0 %	20030506	37.3
	J0955+3954WS	148.99731	39.91079	2.31		16.61	0.0 %	20120119	
J100602.50+071131.80	J1006+0711EN	151.51044	7.19217	2.28	5.6/12.5	16.88	0.0 %	20030102	81.8
	J1006+0711WS	151.50889	7.19195	4.06		16.98	2.1 %	20030422	
J110639.56+433620.64	J1106+4336W	166.66297	43.60582	1.71	4.9/10.5	18.04	0.0 %	20040226	93.4
	J1106+4336E	166.66485	43.60574	1.67		17.33	0.0 %	20040218	
J111519.98+542316.75	J1115+5423EN	168.83326	54.38799	1.94	8.8/11.8	16.33	0.0 %	20030309	48.6
	J1115+5423WS	168.83016	54.38639	1.97		17.64	0.0 %	20030102	
J114411.74+102202.40	J1144+1022EN	176.04894	10.36735	2.17	6.5/14.7	17.69	0.0 %	20030405	12.1
	J1144+1022WS	176.04855	10.36558	2.08		18.48	0.0 %	20120223	
J121418.25+293146.70	J1214+2931EN	183.57607	29.52964	1.45	7.9/9.3	16.08	0.0 %	20060324	60.8
	J1214+2931WS	183.57419	29.52873	1.50		16.87	0.0 %	20130306	
J122217.85-000743.70	J1222-0007EN	185.57438	-0.12881	3.33	4.6/13.5	18.27	1.9 %	20010322	80.5
	J1222-0007WS	185.57308	-0.12903	2.29		18.73	0.2 %	20010401	
J133031.98-003613.80	J1330-0036WN	202.63229	-0.60333	3.47	4.2/4.4	15.48	1.7 %	20000428	116.9
	J1330-0036ES	202.63329	-0.60383	2.64		16.93	5.0 %	20010219	
J133817.27+481632.20	J1338+4816EN	204.57407	48.27806	2.35	10.2/5.6	14.48	0.0 %	20030503	29.2
	J1338+4816WS	204.57200	48.27561	2.10		14.43	0.0 %	20090114	
J150134.72+544734.07	J1501+5447EN	225.39469	54.79280	1.87	3.8/10.7	18.62	0.3 %	20020319	28.7
	J1501+5447WS	225.39373	54.79179	1.78		18.23	0.2 %	20020401	
J151751.77+252353.38	J1517+2523E	229.46573	25.39816	1.75	5.5/7.5	15.63	0.0 %	20110412	96.8
	J1517+2523W	229.46406	25.39834	2.29		19.15	0.2 %	20070522	
J155344.31+302508.50	J1553+3025EN	238.43466	30.41904	1.13	3.5/13.1	18.38	0.0 %	20050413	40.4
	J1553+3025WS	238.43393	30.41830	1.82		21.12	4.1 %	20110705	
J155850.44+272323.93	J1558+2723WN	239.70974	27.39106	1.85	4.1/7.2	19.22	1.6 %	20110527	160.0
	J1558+2723ES	239.71019	27.38998	2.43		16.11	0.1 %	20030702	
J164507.91+205759.43	J1645+2057WN	251.28297	20.96651	1.50	4.2/9.7	18.11	0.0 %	20040611	157.2
	J1645+2057ES	251.28348	20.96543	1.45		17.99	0.0 %	20040524	
J171322.58+325627.90	J1713+3256E	258.34552	32.94121	1.99	4.3/8.0	20.26	1.5 %	20080505	84.6
	J1713+3256W	258.34412	32.94110	1.95		17.23	0.0 %	20020517	
J220635.08+000323.16	J2206+0003WN	331.64572	0.05766	1.75	4.7/4.3	15.97	0.0 %	20030920	159.6
	J2206+0003ES	331.64618	0.05643	1.64		15.97	0.0 %	20031020	

Notes: Column (1): Object name; Column (2): The two optical cores of the system; Column (3) & (4): The right ascension (R.A.) and declination (Decl.) of each core; Column (5): The 80th-percentile of seeing during exposure for each core in arcsecond; Column (6): The separation of two cores in the unit of arcsecond and kpc; Column (7): The SDSS g band magnitude of each core; Column (8): The flux contamination of each core, the values are derived from a Monte Carlo approach (see Section 2 for details); Column (9): The observing date of each spectrum; Column (10): The position angle (PA) of two cores on the sky, in degrees east of north.

and reduction is described in Section 2. The main results are presented in Section 3 and a discussion is given in Section 4. Finally, we summary in Section 5. Cosmological parameters $H_0 = 70 \text{ km s}^{-1} \text{ Mpc}^{-1}$, $\Omega_m = 0.3$, and $\Omega_\Lambda = 0.7$ are adopted throughout the paper and all wavelengths are in vacuum units.

2. DATA & REDUCTION

2.1. The SDSS spectroscopic surveys

The SDSS survey has been running for almost 20 years to create a most detailed map of the Universe (through several phases, SDSS-I: 2000-2005; e.g., York et al. 2000; Abazajian et al. 2003; SDSS-II: 2005-2008; Frieman et al. 2008; SDSS-III: 2008-2014; Eisenstein et al. 2011 and SDSS-IV: 2014-2020; Blanton et al. 2017). So far, multi-color images have been taken almost one third of the sky and more than three million spectra for astronomical objects have been obtained (including almost a million spectra for galax-

ies)⁶. The selected merging galaxies with two optical cores larger than several arcseconds can be spatially resolved by the high quality SDSS images that taken under dark photometric nights with good seeing in five SDSS broad bands (u, g, r, i, z ; Fukugita et al. 1996). The optical spectra data we adopted in the current work were collected from SDSS I to IV and all released in SDSS DR15 (Aguado et al. 2019). The spectra were taken with the double-armed SDSS/BOSS spectrographs with $3''/2''$ fiber aperture covering the whole optical wavelength range. The typical spectral resolving power R is around 2000, corresponding to a native SDSS instrument broadening $\sigma \sim 60 - 70 \text{ km s}^{-1}$ (Smee et al. 2013).

2.2. Sample Selection

⁶ <https://www.sdss.org>

Table 2
BPT classifications

Name	$\log([\text{O III}]/\text{H}\beta)$	$\log([\text{N II}]/\text{H}\alpha)$	$\log([\text{S II}]/\text{H}\alpha)$	$\log([\text{O I}]/\text{H}\alpha)$	BPT _[N II]	BPT _[S II]	BPT _[O I]	Classification
Identified dual AGNs (20 sources)								
J0805+1130EN	–	–	–	–	–	–	–	Type I AGN
J0805+1130WS	–	–	–	–	–	–	–	Type I AGN
J0848+3515EN	0.49 ± 0.02	-0.20 ± 0.05	-0.44 ± 0.02	-1.08 ± 0.03	AGN	Seyfert	Seyfert	Seyfert
J0848+3515WS	–	–	–	–	–	–	–	Type I AGN
J0907+5203EN	0.29 ± 0.00	-0.37 ± 0.01	-0.32 ± 0.00	-0.94 ± 0.01	Comp	Seyfert	Seyfert	Ambiguous AGN
J0907+5203WS	0.71 ± 0.02	-0.33 ± 0.01	-0.29 ± 0.01	-0.85 ± 0.03	AGN	Seyfert	Seyfert	Seyfert
J0914+0853WN	0.35 ± 0.10	0.10 ± 0.01	-0.04 ± 0.02	-0.75 ± 0.04	AGN	LINER	LINER	LINER
J0914+0853ES	–	–	–	–	–	–	–	Type I AGN
J0955+3954EN	-0.05 ± 0.05	-0.34 ± 0.02	-0.30 ± 0.02	-1.01 ± 0.02	Comp	HII	LINER	Ambiguous AGN
J0955+3954WS	0.26 ± 0.01	-0.12 ± 0.01	-0.02 ± 0.01	-0.69 ± 0.02	AGN	LINER	LINER	LINER
J1006+0711EN	–	–	–	–	–	–	–	Type I AGN
J1006+0711WS	–	–	–	–	–	–	–	Type I AGN
J1106+4336W	0.56 ± 0.03	-0.28 ± 0.04	-0.30 ± 0.05	-0.94 ± 0.18	AGN	Seyfert	Seyfert	Seyfert
J1106+4336E	–	–	–	–	–	–	–	Type I AGN
J1115+5423EN	0.84 ± 0.04	-0.18 ± 0.01	-0.38 ± 0.01	-1.10 ± 0.02	AGN	Seyfert	Seyfert	Seyfert
J1115+5423WS	0.88 ± 0.01	-0.33 ± 0.01	-0.41 ± 0.02	-1.25 ± 0.07	AGN	Seyfert	Seyfert	Seyfert
J1144+1022EN	–	–	–	–	–	–	–	Type I AGN
J1144+1022WS	0.31 ± 0.06	0.00 ± 0.01	-0.01 ± 0.01	-0.75 ± 0.05	AGN	LINER	LINER	LINER
J1214+2931EN	0.84 ± 0.05	0.16 ± 0.01	-0.03 ± 0.01	-0.90 ± 0.02	AGN	Seyfert	Seyfert	Seyfert
J1214+2931WS	–	–	–	–	–	–	–	Type I AGN
J1222-0007EN	–	–	–	–	–	–	–	Type I AGN
J1222-0007WS	0.78 ± 0.01	-0.60 ± 0.03	-0.72 ± 0.05	-1.62 ± 0.16	AGN	Seyfert	Seyfert	Seyfert
J1330-0036WN	0.20 ± 0.01	-0.33 ± 0.01	-0.44 ± 0.01	-1.34 ± 0.06	Comp	HII	HII	Comp
J1330-0036ES	0.35 ± 0.02	-0.17 ± 0.02	-0.51 ± 0.01	-1.30 ± 0.02	AGN	HII	Seyfert	Ambiguous AGN
J1338+4816EN	–	–	–	–	–	–	–	Type I AGN
J1338+4816WS	0.40 ± 0.02	-0.26 ± 0.02	-0.44 ± 0.01	-1.30 ± 0.06	AGN	Seyfert	Seyfert	Seyfert
J1501+5447EN	–	–	–	–	–	–	–	Type I AGN
J1501+5447WS	0.11 ± 0.03	-0.10 ± 0.01	-0.38 ± 0.03	-1.29 ± 0.06	Comp	HII	HII	Comp
J1517+2523E	0.61 ± 0.06	0.09 ± 0.04	-0.05 ± 0.03	-0.67 ± 0.04	AGN	LINER	Seyfert	Ambiguous AGN
J1517+2523W	0.36 ± 0.03	0.13 ± 0.02	-0.30 ± 0.05	-0.85 ± 0.05	AGN	Seyfert	Seyfert	Seyfert
J1553+3025EN	–	–	–	–	–	–	–	Type I AGN
J1553+3025WS	0.17 ± 0.03	-0.25 ± 0.02	-0.30 ± 0.05	-0.84 ± 0.05	Comp	LINER	LINER	Ambiguous AGN
J1558+2723WN	–	–	–	–	–	–	–	Type I AGN
J1558+2723ES	–	–	–	–	–	–	–	Type I AGN
J1645+2057WN	0.43 ± 0.02	-0.22 ± 0.02	-0.45 ± 0.02	-1.28 ± 0.03	AGN	Seyfert	Seyfert	Seyfert
J1645+2057ES	0.33 ± 0.01	-0.28 ± 0.01	-0.51 ± 0.01	-1.36 ± 0.02	Comp	HII	HII	Comp
J1713+3256E	0.84 ± 0.09	0.10 ± 0.05	-0.27 ± 0.09	-0.96 ± 0.11	AGN	Seyfert	Seyfert	Seyfert
J1713+3256W	–	–	–	–	–	–	–	Type I AGN
J2206+0003WN	0.01 ± 0.02	-0.07 ± 0.01	-0.17 ± 0.01	-0.89 ± 0.01	Comp	LINER	LINER	Ambiguous AGN
J2206+0003ES	0.28 ± 0.01	0.15 ± 0.02	0.08 ± 0.02	-0.46 ± 0.02	AGN	LINER	LINER	LINER

Notes: BPT_[N II], BPT_[S II], BPT_[O I]: Result of BPT classifications in the $\log([\text{O III}]/\text{H}\beta) - \log([\text{N II}]/\text{H}\alpha)$, $\log([\text{O III}]/\text{H}\beta) - \log([\text{S II}]/\text{H}\alpha)$ and $\log([\text{O III}]/\text{H}\beta) - \log([\text{O I}]/\text{H}\alpha)$ planes, respectively. Seyfert: Seyfert galaxy. Comp: AGN/Starforming composite galaxy. H II: Star-forming region. LINER: Low ionization nuclear emission line region. Ambiguous AGN: AGN of ambiguous classification, i.e. those are classified as one type of AGN in one or two of the BPT diagram(s) and classified as another type of AGN in the remaining diagram(s). Classification: Classification based on BPT diagrams with the SDSS data.

As mentioned in our Paper I and II, we have developed a high efficiency method of systematically searching and identifying dual AGNs from kpc scale merging galaxies and a total of 222 candidates are selected. To select those candidates, we first select merging galaxies that are spatially resolved from the SDSS photometric catalog: galaxies exhibiting two optical cores separated by less than $8''$ and at least one optical core with SDSS fiber spectra (Pâris et al. 2018; Lyke et al. 2020). Secondly, the selected merging galaxies are at least with one radio detection from the FIRST radio survey (Helfand et al. 2015). Typically, enhanced radio power are expected from merge-driven star formations or starbursts (e.g., Bell et al. 2006; Jogee et al. 2009; Robaina et al. 2009). To a certain extent, the requirement of at least one radio detection can help remove the physically unrelated pairs from the merging galaxies sample. Finally, only merging galaxies with at least one core previously identified as an AGN by analyzing SDSS fiber spectra (Pâris et al. 2018) are selected as dual AGN candidates. In this manner, a total of 222 candidates are

selected from the merging galaxies sample. The redshifts of our selected candidates are smaller than 0.25. For candidate with higher redshift, two cores of the kpc merging galaxy may fall in the $2''/3''$ fiber (corresponding to 7.5 or 11.7 kpc at a redshift of 0.25).

In this work, we continue to search and identify dual AGNs based on the SDSS fiber spectra. Doing so, the selected 222 candidates were cross-matched to the database of SDSS DR15 (Aguado et al. 2019) and 61 candidates have been found with both cores observed by the SDSS survey.

For the merging galaxy, the spectra of two cores are not taken at the same time as two fibers on the same plate can't be placed closer than $55''$ and $62''$ due to fiber collisions (e.g., Dawson et al. 2013), respectively, for the original SDSS and the BOSS spectrographs. To explore the nature of activity (e.g., star formation or accretion disk) of each core in the merging system, the contamination from another core should be controlled to a certain low fraction (i.e., 5% here). To do so, we perform a simple simulation to obtain the flux contam-

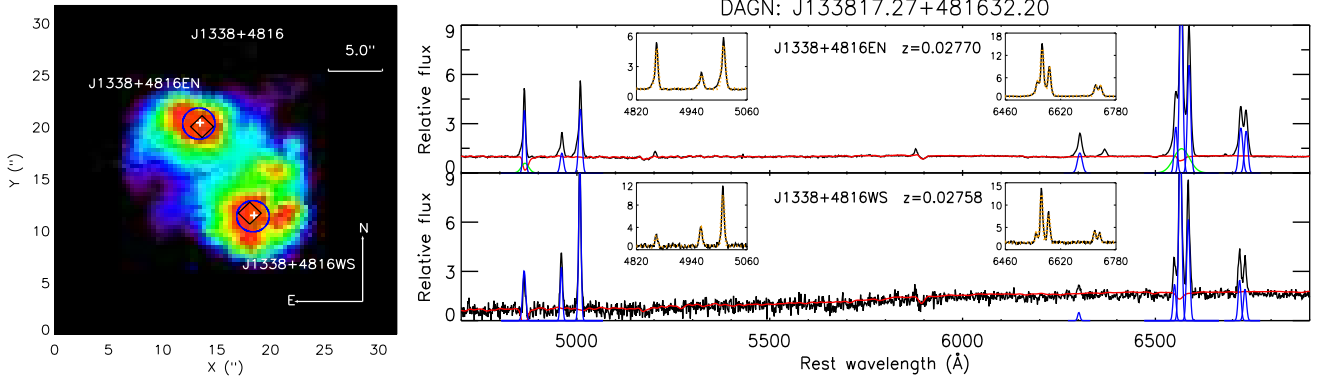


Figure 1. Left: Pseudo color image of J1338+4816 in SDSS g band. The position of the radio detection given in the FIRST catalog is marked by the black diamond. The fiber position of the SDSS spectrum is marked by the blue circle. Right: The spectra of dual AGN: J133817.27+481632.20 respectively for J1338+4816EN (bottom) and J1338+4816WS (top) at rest-frame optical wavelengths. We used pPXF to subtract continuous spectrum and got emission lines of AGN. The red lines represent the continuum component, the blue lines represent the narrow emission lines component and the green lines represent the broad emission lines component.

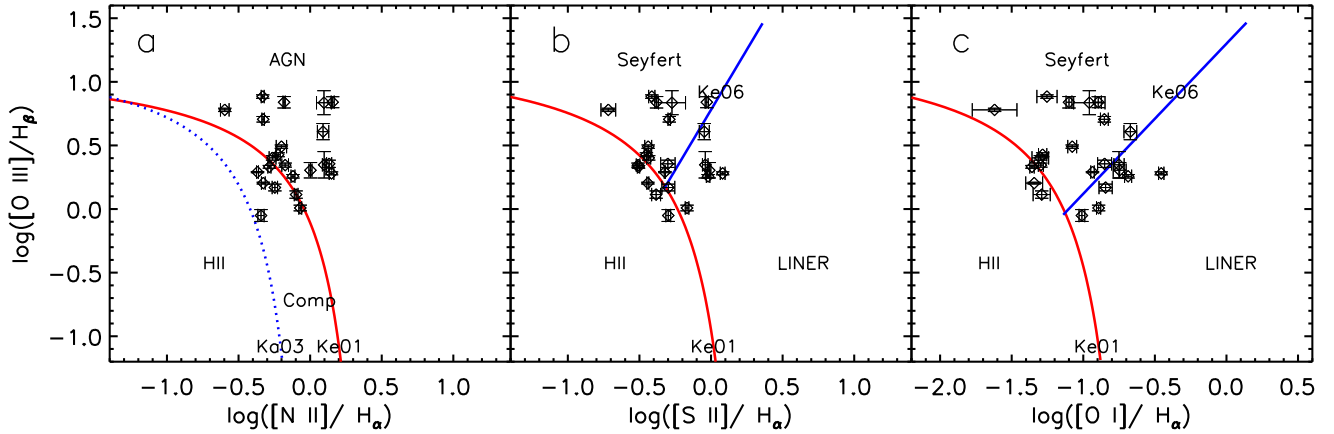


Figure 2. BPT diagram of 23 narrow line AGNs from 20 dual AGNs in the BPT-[N II], BPT-[S II] and BPT-[O I] panels. In panel a, galaxy above the red solid line (Ke01; Kewley et al. 2001) is classified as AGN, below the blue dashed line is purely starforming galaxy (Ka03; Kauffmann et al. 2003), between the red solid line (Ke01) and the blue dashed line (Ka03) is AGN/starforming composite galaxy (Comp). In the AGN region, Seyferts and LINER are, respectively, located above and below the blue solid branch (Ke06; Kewley et al. 2006), as shown in panels b and c. The detail information is presented in Table 2.

ination to each core, by considering the effects of fiber positioning uncertainty and the seeing⁷. In the simulation, the flux of each core is given by g -band magnitude and is assumed to follow a Gaussian distribution spatially with sigma given by the measured seeing. The separation between the two cores is measured from the SDSS g -band images. The aperture size is set to $3''$ and $2''$ if spectra observed by the original SDSS and the BOSS spectrographs, respectively. In this manner, 61 merging galaxies with both cores observed by the SDSS surveys and flux contamination less than 5% are selected as our candidates.

2.3. Subtraction of continuum

The SDSS spectra have already been wavelength and flux calibrated. Before deriving the fluxes of emission lines, the continuum (including absorption features) of the host galaxy should be subtracted properly. To do so, the penalised PiXel Fitting software (pPXF, originally described in Cappellari & Emsellem 2004 and upgraded in Cappellari 2017) was adopted to fit the continuum and absorption features. We operated the pPXF with stellar template of MILES

Library (Sánchez-Blázquez et al. 2006). This library contains 985 flux well-calibrated stars with wavelength coverage from 3525 \AA to 7500 \AA , at a spectral resolution of $\text{FWHM} \sim 2.51 \text{ \AA}$, $\sigma \sim 64 \text{ km s}^{-1}$, slightly higher than the SDSS's spectral resolution. These templates are properly convolved in pPXF to the resolution of SDSS spectra before fitting. All prominent emission lines were masked when subtracting the continuum and absorption features. As an example, we show the performance of this subtraction in Fig. 1 for J1338+4816 system (as well as in the Appendix A for more examples).

2.4. The fitting of emission lines

By properly subtracting the continuum and absorption features of host galaxy, we now perform emission line measurements using a IDL code developed in the current work. In total, 9 strong optical emission lines (i.e., $H\beta$, $[\text{O III}] \lambda\lambda 4959, 5007$, $[\text{O I}] \lambda 6300$, $H\alpha$, $[\text{N II}] \lambda\lambda 6549, 6583$, $[\text{S II}] \lambda\lambda 6717, 6731$) are fitted, and their properties, i.e., FWHMs, central wavelength, flux, are measured. We note that the derived FWHMs of those emission lines have been subtracted the instrumental broadening ($\text{FWHM} \sim 2.76 \text{ \AA}$). The fluxes of emission lines have been corrected for the foreground Galactic extinction using the extinction map of Schlegel et al.

⁷ The 80th-percentile of seeing is adopted here.

Table 3
Identified dual AGNs

DAGN	AGN	Z_{sdss}	FWHM_{NLR} (km s^{-1})	$\text{FWHM}_{\text{H}\beta}$ (km s^{-1})	$\text{FWHM}_{\text{H}\alpha}$ (km s^{-1})	V_{offset} (km s^{-1})	Sep kpc	$W_1 - W_2$ mag	Radio	Classification
J080544.13+113040.30	J0805+1130EN	0.19738	492 ± 23	1635 ± 34	3275 ± 37	540 ± 15	10.8	0.692	Y	Type I AGN
	J0805+1130WS	0.19918	931 ± 12	2612 ± 126	5388 ± 17					Type I AGN
J084809.69+351532.12	J0848+3515EN	0.05727	333 ± 30	489 ± 22	492 ± 13	90 ± 15	6.2	0.632	Y	Seyfert
	J0848+3515WS	0.05697	677 ± 14	1788 ± 65	2664 ± 15					Type I AGN
J090714.61+520350.61	J0907+5203EN	0.06024	462 ± 13	453 ± 23	440 ± 13	207 ± 4	8.5	0.429	Y	Ambiguous AGN
	J0907+5203WS	0.05955	406 ± 16	373 ± 28	407 ± 14			0.368	Y	Seyfert
J091448.94+085324.45	J0914+0853WN	0.13997	763 ± 23	460 ± 43	575 ± 15	18 ± 11	9.4	0.184	Y	LINER
	J0914+0853ES	0.13991	359 ± 29	1404 ± 23	2071 ± 13			0.792		Type I AGN
J095559.35+395438.87	J0955+3954EN	0.04876	291 ± 20	305 ± 35	280 ± 21	159 ± 4	9.7	0.481	Y	Ambiguous AGN
	J0955+3954WS	0.04929	520 ± 11	516 ± 20	519 ± 11				Y	LINER
J100602.50+071131.80	J1006+0711EN	0.12051	785 ± 12	970 ± 40	2121 ± 15	399 ± 8	12.5	1.194	Y	Type I AGN
	J1006+0711WS	0.12184	987 ± 15	1000 ± 41	2547 ± 23					Type I AGN
J110639.56+433620.64	J1106+4336W	0.12473	460 ± 21	530 ± 22	560 ± 18	141 ± 11	10.5	0.782	Y	Seyfert
	J1106+4336E	0.12426	595 ± 17	1335 ± 41	3943 ± 12					Type I AGN
J111519.98+542316.75	J1115+5423EN	0.07043	526 ± 18	549 ± 29	516 ± 11	264 ± 4	11.8	0.787	Y	Seyfert
	J1115+5423WS	0.07131	361 ± 27	375 ± 28	320 ± 18					Seyfert
J114411.74+102202.40	J1144+1022EN	0.12594	496 ± 20	3440 ± 13	3401 ± 13	189 ± 11	14.7	1.003	Y	Type I AGN
	J1144+1022WS	0.12531	479 ± 20	371 ± 36	486 ± 11			0.128		LINER
J121418.25+293146.70	J1214+2931EN	0.06326	618 ± 17	571 ± 25	517 ± 11	72 ± 9	9.3	0.059	Y	Seyfert
	J1214+2931WS	0.06350	444 ± 22	1410 ± 167	2405 ± 16			1.274		Type I AGN
J122217.85-000743.70	J1222-0007EN	0.17290	792 ± 12	1295 ± 50	2000 ± 22	246 ± 13	13.5	1.296	Y	Type I AGN
	J1222-0007WS	0.17208	380 ± 26	480 ± 22	348 ± 16					Seyfert
J133031.98-003613.80	J1330-0036WN	0.05424	280 ± 23	324 ± 32	297 ± 19	24 ± 4	4.4	0.598	Y	Comp
	J1330-0036ES	0.05416	521 ± 19	353 ± 29	348 ± 16					Ambiguous AGN
J133817.27+481632.20	J1338+4816EN	0.02770	566 ± 15	1819 ± 34	2214 ± 18	36 ± 9	5.6	0.590	Y	Type I AGN
	J1338+4816WS	0.02758	419 ± 16	554 ± 19	423 ± 13				Y	Seyfert
J150134.72+544734.07	J1501+5447EN	0.16421	560 ± 17	1435 ± 149	2502 ± 18	168 ± 8	10.7	0.897	Y	Type I AGN
	J1501+5447WS	0.16365	452 ± 23	426 ± 25	410 ± 14					Comp
J151751.77+252353.38	J1517+2523E	0.07125	575 ± 17	619 ± 22	885 ± 13	225 ± 13	7.5	0.256	Y	Ambiguous AGN
	J1517+2523W	0.07050	473 ± 21	343 ± 30	399 ± 14					Seyfert
J155344.31+302508.50	J1553+3025EN	0.23699	936 ± 10	3091 ± 35	3616 ± 12	222 ± 8	13.1	1.195	Y	Type I AGN
	J1553+3025WS	0.23773	667 ± 15	477 ± 22	523 ± 11					Ambiguous AGN
J155850.44+272323.93	J1558+2723WN	0.09517	636 ± 11	1283 ± 16	1936 ± 18	492 ± 15	7.2	0.658	Y	Type I AGN
	J1558+2723ES	0.09353	663 ± 13	1037 ± 55	1890 ± 36					Type I AGN
J164507.91+205759.43	J1645+2057WN	0.13004	428 ± 23	526 ± 20	511 ± 12	252 ± 7	9.7	0.569	Y	Seyfert
	J1645+2057ES	0.13088	333 ± 30	364 ± 29	346 ± 17			0.569		Comp
J171322.58+325627.90	J1713+3256E	0.10141	358 ± 28	540 ± 38	419 ± 19	51 ± 15	8.0	0.631	Y	Seyfert
	J1713+3256W	0.10158	458 ± 21	5008 ± 19	5166 ± 17					Type I AGN
J220635.08+000323.16	J2206+0003WN	0.04657	392 ± 25	320 ± 32	329 ± 17	129 ± 7	4.3	0.107	Y	Ambiguous AGN
	J2206+0003ES	0.04614	615 ± 16	511 ± 20	590 ± 12					LINER

Notes: Z_m : The redshift is from the median of main strong emission lines that having higher S/N. FWHM_{NLR} : The FWHM of narrow line region is measured from [O III] $\lambda 5007$ line. FWHM_{BLR} : The FWHM of broad line region is measured from H α broad line component. V_{offset} : The velocity offset of two AGN cores. Sep: The separation of two AGN optical cores. $W_1 - W_2$: The color between W_1 and W_2 bands for the resolved or unresolved core(s) from WISE. Classification: The classification of two AGN optical cores. For Type II AGN, we classify them based on the BPT diagrams (see Fig. 2 and Table 2) and for Type I AGN, we identify them by the value of FWHM of H α or H β .

(1998) and then the local reddening using the measured Balmer decrement⁸.

When fitting the emission lines, for example, we set one Gaussian for [N II] $\lambda 6549$ line, one Gaussian for [N II] $\lambda 6583$ line, two Gaussians with the same central wavelength respectively for H α broad and narrow line components. When H α emission line does not have broad line component, we then set only one Gaussian for it. The fitting process of other emission lines are similar. In Fig. 1 (as well as in the Appendix A), examples of the fitting are shown.

3. RESULTS & DISCUSSIONS

3.1. Identify AGN

In this paper, we adopt the same criteria to identify Type I and II AGNs as described in our Paper II. Type I AGN is usu-

⁸ The intrinsic, dust-free Balmer decrement of H α /H β ratio of 3.1 is adopted here (Osterbrock 1989).

ally distinguished by the FWHM of the H α broad line component: 1) FWHM of broad H α $> 2200 \text{ km s}^{-1}$; or 2) FWHM of broad H α $> 1200 \text{ km s}^{-1}$ and $h(\text{broad H}\alpha)/h(\text{narrow H}\alpha) > 0.1$, where $h(\text{broad H}\alpha)$ and $h(\text{narrow H}\alpha)$ are the heights of H α broad and narrow line components, respectively. The height of H α emission line is derived from the peak of the Gaussian fits. The detail criteria of Type I AGN has been described in the work of Hao et al. (2005).

For the Type II AGNs, we use the Baldwin-Phillips-Terlevich (BPT; Baldwin et al. 1981, Kewley et al. 2001, Kauffmann et al. 2003, Kewley et al. 2006) diagrams to identify them, using emission line flux ratios, i.e., [O III] $\lambda 5007/\text{H}\beta$, [N II] $\lambda 6583/\text{H}\alpha$, [S II] $\lambda \lambda 6717, 6731/\text{H}\alpha$, and [O I] $\lambda 6300/\text{H}\alpha$. With the fluxes of emission lines measured in Section 2.4, we show the positions of our final dual AGNs in the three BPT panels (BPT-[N II], BPT-[S II] and BPT-[O I], see Fig. 2). The fluxes used here have been corrected for reddening and extinction effects. Based on the classifications on

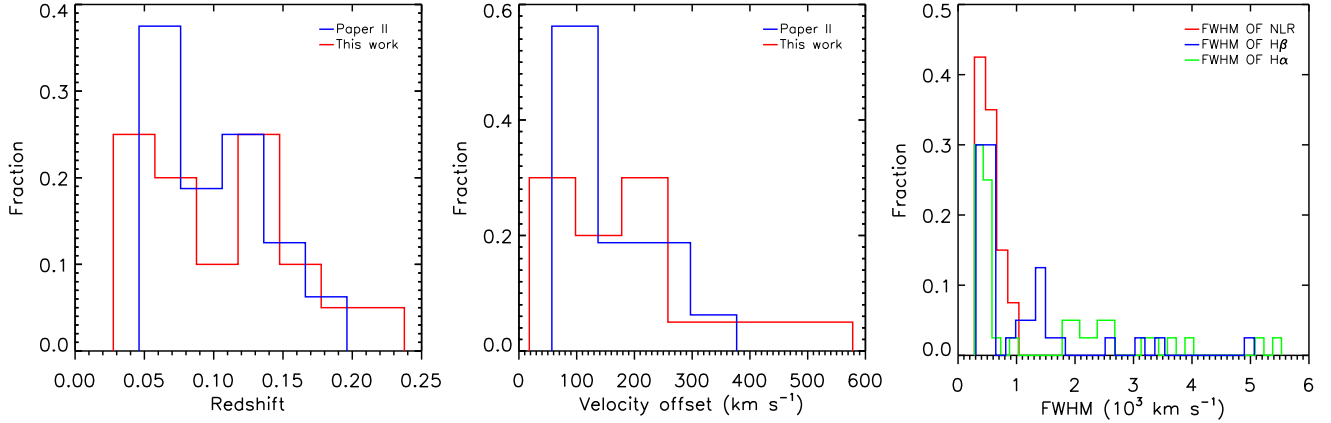


Figure 3. Left: redshift distribution of dual AGNs; Middle: the distribution of velocity offset of dual AGNs; Right: FWHM distribution of dual AGNs.

BPT diagrams (see Kewley et al. 2006 for more details), the Type II AGN can be further divided into the AGN/starforming composite galaxies (Comp), the Seyfert galaxies (Seyfert), the ambiguous galaxies (ambiguous AGN) and the Low ionization nuclear emission line region (LINER). Ambiguous galaxies/AGNs are those that classified as one subtype of object in one or two of the BPT panel(s) but classified as another subtype of object in the remaining BPT panel(s). Finally, we remark that the diagnostics purely based on optical line ratios can not provide secure classification of the nature of the systems with narrow line emission lines (especially, those systems classified as LINERs⁹, composite galaxies and ambiguous galaxies/AGNs). Radio/X-ray follow-up observations of those dual AGN candidates are further required to provide more stringent constraints on their natures of the nuclei activities.

3.2. The identified dual AGNs sample

Using the criteria mentioned above, 20 dual AGNs are finally identified based on the fiber spectra from the SDSS survey. The efficiency of this systematic searching is about 32.79% (20/61). If excluding those systems containing LINERs, composite galaxies and ambiguous galaxies/AGNs (their activity natures requiring further observations), the systematic searching efficiency is still as high as 16.39% (10/61). The observation information of these 20 dual AGNs is shown in Table 1. We note that 5 of 20 dual AGNs (J0848+3515, J0907+5203, J1214+2931, J1645+2057, J2206+0003) have been confirmed with the long-slit spectroscopy by using YFOSC mounted on LJT of Yunnan observatories (Paper II) separately. The properties (e.g., FWHM, velocity offset, emission line ratios and activity nature) of the five dual AGN revealed by the SDSS fiber spectra here are consistent with those measured by the long-slit spectra in our Paper II very well.

In the 20 dual AGNs, about 40.0% (16/40) are Type I AGNs, about 7.5% (3/40) are classified as Comps, about 27.5% (11/40) are classified as Seyferts, about 10.0% (4/40) are LINERs, and about 15.0% (6/40) are ambiguous galaxies/AGNs. The detail classifications of our dual AGNs are presented in Table 2.

⁹ The origin of LINER is still on hot debate. Most of the LINERs are likely to be AGNs (e.g., Heckman & Best 2014; Netzer 2015) while the contribution from evolved post-AGB stars and low-mass X-ray binaries can not be ruled out (e.g., Ho 2008; Sarzi et al. 2010; Cid Fernandes et al. 2011; Capetti & Baldi 2011; Yan & Blanton 2012).

The redshift of those 20 dual AGN candidates ranges from 0.02758 to 0.23699 with a median value of 0.10158 shown in the left of Fig. 3. Compared to the dual AGN sample constructed by the long-slit spectroscopy by the LJT (Paper II), the redshift distribution of the current work is more flat along the redshift. In the middle panel of Fig. 3, the velocity offset are ranging from 18 km s⁻¹ to 540 km s⁻¹ with a median value of 168 km s⁻¹. The distribution of velocity offset is consistent with that of previous work (e.g., Liu et al. 2011, Comerford et al. 2013).

In the right panel of Fig. 3, the FWHM from [O III] λ 5007 line (red line) for NLRs and from H α (blue line) and H β (green line) lines for BLRs are shown. The detail values can be checked from Table 3. The current dual AGNs, together with those from our Paper II and previous literature, are shown in the redshift versus projected separation plane in Fig. 4. Similar to our Paper II, the current dual AGNs are just right to fill the gap and largely improve completeness of the redshift distribution of dual AGNs.

Finally, the infrared color $W_1 - W_2$ distribution is shown in Fig. 5 for the dual AGNs. Similar to the result of our Paper II, Type I and II AGNs show quite distinct distribution in $W_1 - W_2$ color, with the Type I AGN more redder while Type II more bluer.

4. REMARKS ON INDIVIDUAL INTERESTING OBJECTS

In the current work, 20 dual AGNs were identified by the analysis of the SDSS fiber spectra. For these dual AGNs, more solid evidences are required to confirm their nuclei natures, e.g., from the high angular resolution radio or X-ray imaging observations (e.g., Fu et al. 2011b; Liu et al. 2013). Although no new follow-up observations in radio/X-ray bands, we check the images of these dual AGNs from the existing archival data, e.g., the FIRST survey (Helfand et al. 2015) and the Chandra Data Archive¹⁰.

Interestingly, two of our dual AGNs, i.e., J0955 + 3954 and J1338 + 4816, are found to show two prominent radio detections in FIRST images (see Figs. 6 and 7). The central positions of the two radio detections are in great agreement with the SDSS optical central positions. The integrated fluxes at 1.4 GHz given by the FIRST survey are 12.24 ± 0.13 mJy and 2.57 ± 0.13 mJy, corresponding to rest frame $P_{1.4\text{GHz}}$ of $(6.77 \pm 0.07) \times 10^{22}$ W Hz⁻¹ and

¹⁰ <https://cxc.harvard.edu/cda/>

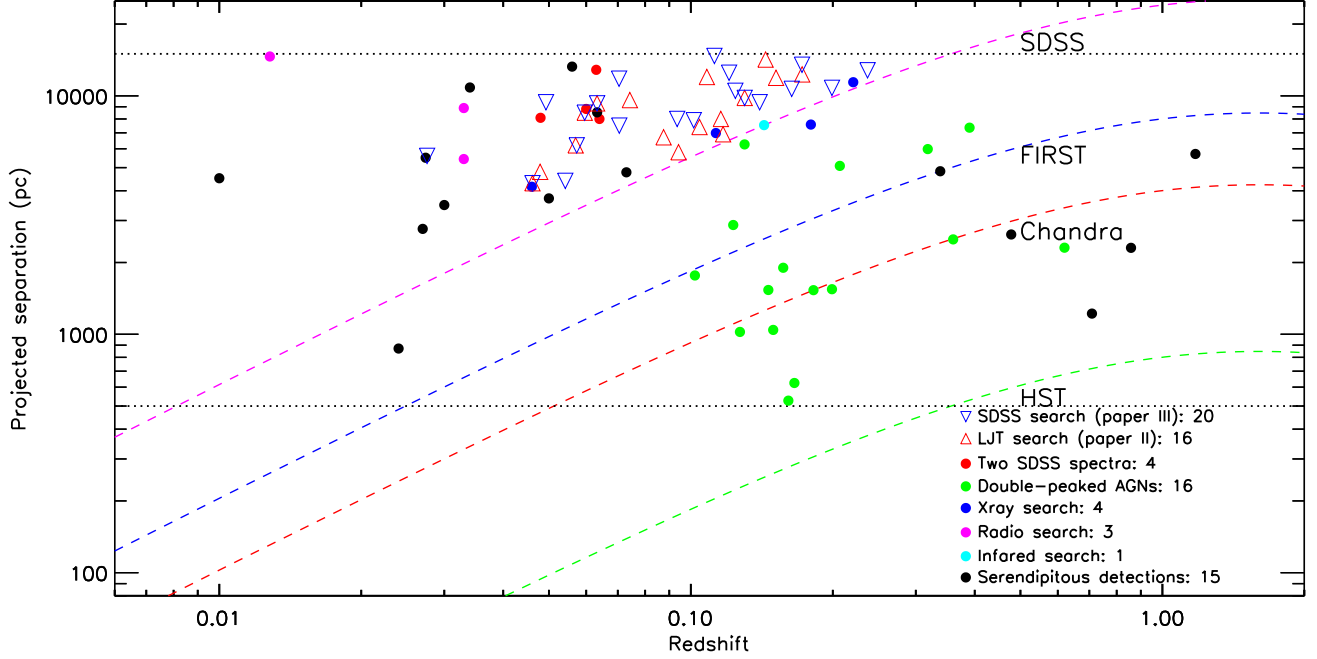


Figure 4. Identified dual AGNs in this work comparing with the known confirmed dual AGNs in paper II and other works. In this work, we have found 20 dual AGNs (15 dual AGNs are newly identified and 5 dual AGNs are already confirmed in paper II). The magenta, blue, red, green dashed lines, respectively, represent the critical resolutions of SDSS spectroscopy, FIRST, Chandra, HST catalogs, i.e., $3.0''$, $1.0''$, $0.5''$, $0.1''$, respectively. The two horizontal dashed lines are the typical separations, i.e., 0.5 and 15 kpc, of dual AGNs, respectively. The 43 known dual AGNs are found by the following methods: (1) Two SDSS spectra, (2) Double-peaked AGNs, (3) X-ray search, (4) Radio search, (5) Infrared search and (6) Serendipitous detections. These methods here simply indicate how the dual AGNs were originally identified. References for the 43 known dual AGNs: (1) Junkkarinen et al. 2001; (2) Komossa et al. 2003; (3) Ballo et al. 2004; (4) Guainazzi et al. 2005; (5) Gerke et al. 2007; (6) Barth et al. 2008; (7) Bianchi et al. 2008; (8) Comerford et al. 2009a; (9) Comerford et al. 2009b; (10) Piconcelli et al. 2010; (11) Comerford et al. 2011; (12) Fu et al. 2011b; (13) Koss et al. 2011; (14) Liu et al. 2011; (15) McGurk et al. 2011; (16) Shen et al. 2011; (17) Barrows et al. 2012; (18) Fu et al. 2012; (19) Frey et al. 2012; (20) Koss et al. 2012; (21) Teng et al. 2012; (22) Mazzarella et al. 2012; (23) Liu et al. 2013; (24) Huang et al. 2014; (25) Comerford et al. 2015; (26) Fu et al. 2015a; (27) Müller-Sánchez et al. 2015; (28) Ellison et al. 2017; (29) Secrest et al. 2017; (30) Liu et al. 2018.

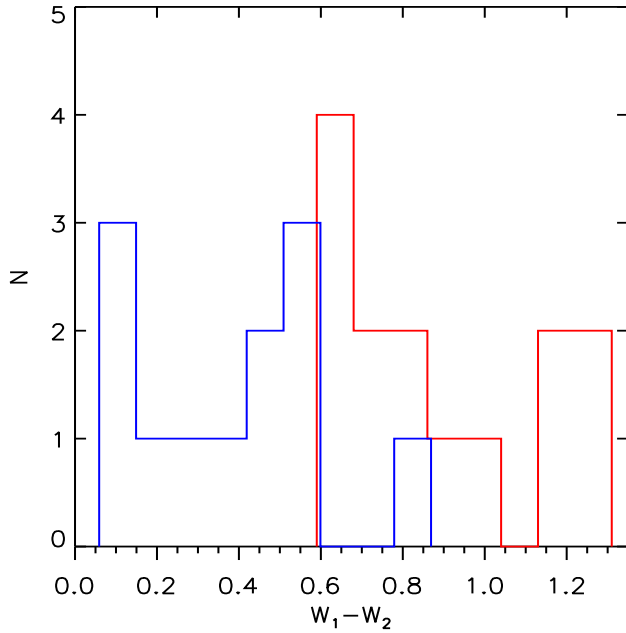


Figure 5. Distribution of W_1-W_2 values of dual AGNs, the red histogram represents Type I AGN or the dual AGNs including at least one Type I AGN and the blue one represents Type II AGN or the dual AGNs without Type I AGN.

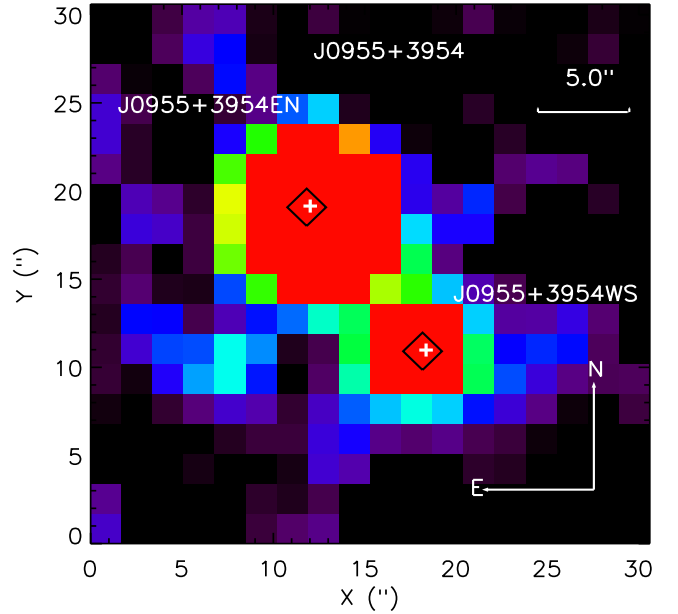


Figure 6. FIRST 1.4 GHz pseudo-color image of J0955 + 3954 on a logarithmic scale. The two nuclei, i.e., J0955 + 3954EN and J0955 + 3954WS, are clearly resolved, with the central positions marked by the black diamonds. The white pluses here mark the optical positions from the SDSS images. North is up and east is to the left. Spatial scale is also shown in the top-right corner.

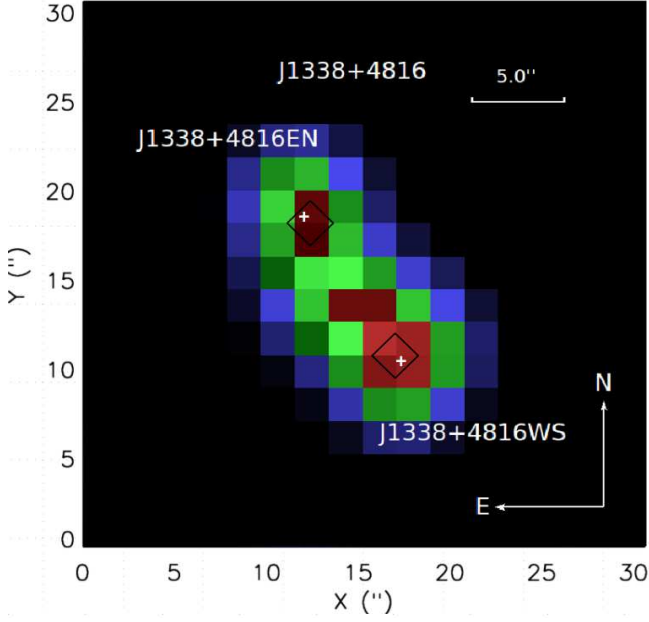


Figure 7. Similar to Fig. 6 but for J1338 + 4861.

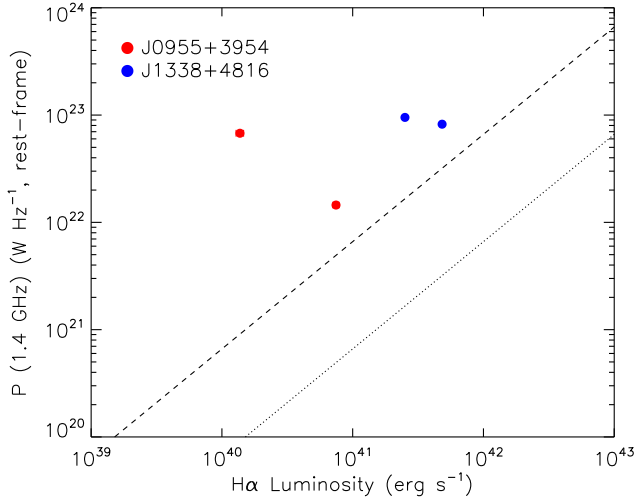


Figure 8. Rest-frame 1.4 GHz radio power versus $H\alpha$ luminosity for J0955 + 3954 (red dots) and J1338 + 4816 (blue dots) systems. Dotted line indicate radio-derived star formation rates (SFRs) equal to the $H\alpha$ -derived SFRs (using the relations from Hopkins et al. 2001), while the dashed line mark the former 10 times larger than the latter.

$(1.45 \pm 0.07) \times 10^{22} \text{ W Hz}^{-1}$, for J0955 + 3954EN and J0955 + 3954WS, respectively. For J1338 + 4816EN and J1338 + 4816WS, the integrated fluxes are, respectively, $47.20 \pm 0.14 \text{ mJy}$ and $55.05 \pm 0.14 \text{ mJy}$, corresponding to rest frame $P_{1.4\text{GHz}}$ of $(8.22 \pm 0.02) \times 10^{22} \text{ W Hz}^{-1}$ and $(9.51 \pm 0.02) \times 10^{22} \text{ W Hz}^{-1}$. When deriving the rest frame 1.4 GHz luminosity, a mean spectral index of -0.7 is assumed (e.g., Pushkarev & Kovalev 2012, Hovatta et al. 2014).

To show the radio power from AGN activities, the $P_{1.4\text{GHz}}$ versus $L_{H\alpha}$ (good indicator of star formation rate) diagram of the two systems is shown in Fig. 8. Clearly, both cores of the two systems have radio powers 10 times larger than those expected from the $H\alpha$ -traced SFR, indicating significant

radio-excess powers from AGN activities. The above results provide unambiguous evidences of the AGN nature of the two dual AGNs.

5. CONCLUSIONS

1. We have carried a systematic search for dual AGNs from 61 merging galaxies by using the SDSS fiber spectra. 20 dual AGNs are finally identified by the careful analysis of their emission lines. The successful efficiency is about 33%, similar to that of our Paper II. For the 20 dual AGNs, 15 are discovered for the first time and the remaining 5 systems have been discovered in our Paper II.
2. Interestingly, 2 of the identified dual AGNs show clear two radio cores in FIRST 1.4 GHz images. Compared to the $H\alpha$ luminosities of the two systems, both cores of the two dual AGNs are the so-called radio-excess AGN.
3. With the efforts from Paper II and the current work, we have constructed a large sample of 31 dual AGNs. This sample, together with more candidates from future observations, will provide important constraints on understanding AGN physics and the coevolution between the supermassive black holes and their host galaxies.

ACKNOWLEDGEMENTS

We acknowledge the support of the staff of the Lijiang 2.4-m telescope. Funding for the telescope has been provided by CAS and the People's Government of Yunnan Province. The work of J. M. Bai is supported by the NSFC (grants 11133006, 11361140347) and the Strategic Priority Research Program "The Emergence of Cosmological Structures" of the Chinese Academy of Sciences (grant No. XDB09000000). Y. Huang and X.-W. Liu acknowledge support by the National Key Basic Research Program of China 2014CB845700. We thank XX for help.

Facilities: SDSS (SDSS spectrograph), LJT (Lijiang 2.4-m telescope), LAMOST (Large Sky Area Multi-Object Fiber Spectroscopy Telescope), FIRST (Faint Images of the Radio Sky at Twenty-Centimeters)

REFERENCES

- Abazajian, K., Adelman-McCarthy, J. K., Agüeros, M. A., et al. 2003, *AJ*, 126, 2081
- Aguado, D. S., Ahumada, R., Almeida, A., et al. 2019, *ApJS*, 240, 23
- Arzoumanian, Z., Brazier, A., Burke-Spolaor, S., et al. 2016, *ApJ*, 821, 13
- Baldwin, J. A., Phillips, M. M., & Terlevich, R. 1981, *PASP*, 93, 5
- Ballo, L., Braitto, V., Della Ceca, R., et al. 2004, *ApJ*, 600, 634
- Barth, A. J., Bentz, M. C., Greene, J. E., & Ho, L. C. 2008, *ApJ*, 683, L119
- Begelman M. C., Blandford R. D., Rees M. J., 1980, *Nature*, 287, 307
- Bell, E. F., Phleps, S., Somerville, R. S., et al. 2006, *ApJ*, 652, 270
- Bianchi, S., Chiaberge, M., Piconcelli, E., Guainazzi, M., & Matt, G. 2008, *MNRAS*, 386, 105
- Blanton, M. R., Bershady, M. A., Abolfathi, B., et al. 2017, *AJ*, 154, 28
- Barrows, R. S., Stern, D., Madsen, K., et al. 2012, *ApJ*, 744, 7
- Cappellari, M. & Emsellem, E. 2004, *PASP*, 116, 138
- Cappellari, M. 2017, *MNRAS*, 466, 798
- Capetti, A. & Baldi, R. D. 2011, *A&A*, 529, A126
- Cid Fernandes, R., Stasińska, G., Mateus, A., et al. 2011, *MNRAS*, 413, 1687
- Colpi M., Dotti M., 2011, *ASdv. Sci. Lett.*, 4, 181
- Comerford, J. M., Gerke, B. F., Newman, J. A., Davis, M., Yan, R., Cooper, M. C., Faber, S. M., Koo, D. C., Coil, A. L., Rosario, D. J., & Dutton, A. A. 2009a, *ApJ*, 698, 956
- Comerford, J. M., Griffith, R. L., Gerke, B. F., Cooper, M. C., Newman, J. A., Davis, M., & Stern, D. 2009b, *ApJ*, 702, L82
- Comerford, J. M., Pooley, D., Gerke, B. F., & Madejski, G. M. 2011, *ApJ*, 737, L19+
- Comerford, J. M., Gerke, B. F., Stern, D., et al. 2012, *ApJ*, 753, 42
- Comerford, J. M., Schluns, K., Greene, J. E., & Cool, R. J. 2013, *ApJ*, 777, 64
- Comerford, J. M., Pooley, D., Barrows, R. S., et al. 2015, *ApJ*, 806, 219
- Dawson, K. S., Schlegel, D. J., Ahn, C. P., et al. 2013, *AJ*, 145, 10
- Ellison, S. L., Secrest, N. J., Mendel, J. T., et al. 2017, *MNRAS*, 470, L49
- Eisenstein, D. J., Weinberg, D. H., Agol, E., et al. 2011, *AJ*, 142, 72
- Frey, S., Paragi, Z., An, T., et al. 2012, *MNRAS*, 425, 1185
- Frieman, J. A., Bassett, B., Becker, A., et al. 2008, *AJ*, 135, 338
- Fu, H., Zhang, Z.-Y., Assef, R. J., et al. 2011b, *ApJ*, 740, L44
- Fu, H., Yan, L., Myers, A. D., et al. 2012, *ApJ*, 745, 67
- Fu, H., Myers, A. D., Djorgovski, S. G., et al. 2015a, *ApJ*, 799, 72
- Fukugita, M., Ichikawa, T., Gunn, J. E., et al. 1996, *AJ*, 111, 1748
- Gerke, B. F., et al. 2007, *ApJ*, 660, L23
- Goulding, A. D., Pardo, K., Greene, J. E., et al. 2019, *ApJ*, 879, L21
- Guainazzi, M., Piconcelli, E., Jiménez-Bailón, E., & Matt, G. 2005, *A&A*, 429, L9
- Hao, L., et al. 2005, *AJ*, 129, 1783
- Heckman, T. M. & Best, P. N. 2014, *ARA&A*, 52, 589
- Helfand, D. J., White, R. L., & Becker, R. H. 2015, *ApJ*, 801, 26
- Ho, L. C. 2008, *ARA&A*, 46, 475
- Hopkins, A. M., Connolly, A. J., Haarsma, D. B., et al. 2001, *AJ*, 122, 288
- Hopkins P. F., Hernquist L., Cox T. J., Kereš D., 2008, *ApJS*, 175, 356
- Hovatta, T., Aller, M. F., Aller, H. D., et al. 2014, *AJ*, 147, 143
- Huang, Y., Liu, X.-W., Yuan, H.-B., et al. 2014, *MNRAS*, 439, 2927
- Jogee, S., Miller, S. H., Penner, K., et al. 2009, *ApJ*, 697, 1971
- Junkkarinen V., Shields G. A., Beaver E. A., Burbidge E. M., Cohen R. D., Hamann F., Lyons R. W., 2001, *ApJ*, 549, 155
- Kauffmann, G., Heckman, T. M., Tremonti, C., et al. 2003, *MNRAS*, 346, 1055
- Kewley, L. J., Dopita, M. A., Sutherland, R. S., Heisler, C. A., & Trevena, J. 2001, *ApJ*, 556, 121
- Kewley, L. J., Groves, B., Kauffmann, G., & Heckman, T. 2006, *MNRAS*, 372, 961
- Kelly, B. C. & Shen, Y. 2013, *ApJ*, 764, 45
- Kormendy, J., & Richstone, D. 1995, *ARA&A*, 33, 581
- Kormendy, J., & Ho, L. C. 2013, *ARA&A*, 51, 511
- Komossa S., Burwitz V., Hasinger G., Predehl P., Kaastra J. S., Ikebe Y., 2003, *ApJ*, 582L, 15
- Komossa, S., & Zensus, J. A. 2016, in *IAU Symposium*, Vol. 312, IAU Symposium, ed. Y. Meiron, S. Li, F.-K. Liu, & R. Spurzem, 13–25
- Koss, M., Mushotzky, R., Treister, E., Veilleux, S., Vasudevan, R., Miller, N., Sanders, D. B., Schawinski, K., & Trippe, M. 2011, *ApJ*, 735, L42+
- Koss, M., Mushotzky, R., Treister, E., et al. 2012, *ApJ*, 746, L22
- Koss, M. J., Glidden, A., Baloković, M., et al. 2016, *ApJ*, 824, L4
- Liu, X., Greene, J. E., Shen, Y., & Strauss, M. A. 2010a, *ApJ*, 715, L30
- Liu, X., Shen, Y., Strauss, M. A., & Hao, L. 2011, *ApJ*, 737, 101
- Liu, X., Civano, F., Shen, Y., et al. 2013, *ApJ*, 762, 110
- Liu, X., Lazio, T. J. W., Shen, Y., & Strauss, M. A. 2018, *ApJ*, 854, 169
- Lyke, B. W., Higley, A. N., McLane, J. N., et al. 2020, *ApJS*, 250, 8
- Mazzarella, J. M., Iwasawa, K., Vavilkin, T., et al. 2012, *AJ*, 144, 125
- McGurk, R. C., Max, C. E., Rosario, D. J., Shields, G. A., Smith, K. L., & Wright, S. A. 2011, *ApJ*, 738, L2
- Müller-Sánchez, F., Comerford, J. M., Nevin, R., et al. 2015, *ApJ*, 813, 103
- Netzer, H. 2015, *ARA&A*, 53, 365
- Nevin, R., Comerford, J., Müller-Sánchez, F., Barrows, R., & Cooper, M. 2016, *ApJ*, 832, 67
- Osterbrock, D. E. 1989, *Astrophysics of Gaseous Nebulae and Active Galactic Nuclei*. University Science Books, Mill Valley, CA
- Pàris, I., Petitjean, P., Aubourg, É., et al. 2018, *A&A*, 613, A51
- Piconcelli, E., et al. 2010, *ApJ*, 722, L147
- Pushkarev, A. B. & Kovalev, Y. Y. 2012, *A&A*, 544, A34
- Robaina, A. R., Bell, E. F., Skelton, R. E., et al. 2009, *ApJ*, 704, 324
- Rodriguez, C., Taylor, G. B., Zavala, R. T., et al. 2006, *ApJ*, 646, 49
- Sánchez-Blázquez, P., Peletier, R. F., Jiménez-Vicente, J., et al. 2006, *MNRAS*, 371, 703
- Sarzi, M., Shields, J. C., Schawinski, K., et al. 2010, *MNRAS*, 402, 2187
- Satyapal, S., Ellison, S. L., McAlpine, W., et al. 2014, *MNRAS*, 441, 1297
- Satyapal, S., Secrest, N. J., Ricci, C., et al. 2017, *ApJ*, 848, 126
- Schlegel, D. J., Finkbeiner, D. P., & Davis, M. 1998, *ApJ*, 500, 525
- Secrest, N. J., Schmitt, H. R., Blecha, L., Rothberg, B., & Fischer, J. 2017, *ApJ*, 836, 183
- Shen, Y., Liu, X., Greene, J. E., & Strauss, M. A. 2011, *ApJ*, 735, 48
- Smee, S. A., Gunn, J. E., Uomoto, A., et al. 2013, *AJ*, 146, 32
- Smith, K. L., Shields, G. A., Bonning, E. W., McMullen, C. C., Rosario, D. J., & Salvander, S. 2010, *ApJ*, 716, 866
- Teng, S. H., et al. 2012, *ApJ*, 753, 165
- Volonteri, M., Haardt, F., & Madau, P. 2003, *ApJ*, 582, 559
- Wang, J.-M., Chen, Y.-M., Hu, C., et al. 2009, *ApJ*, 705, L76
- Yan, R. & Blanton, M. R. 2012, *ApJ*, 747, 61
- York, D. G., Adelman, J., Anderson, J. E., et al. 2000, *AJ*, 120, 1579
- Yu Q. -J., Lu Y. -J., Mohayaee R., Colin, J., 2011, *ApJ*, 738, 92

APPENDIX

A. NOTES FOR INDIVIDUAL DUAL AGN

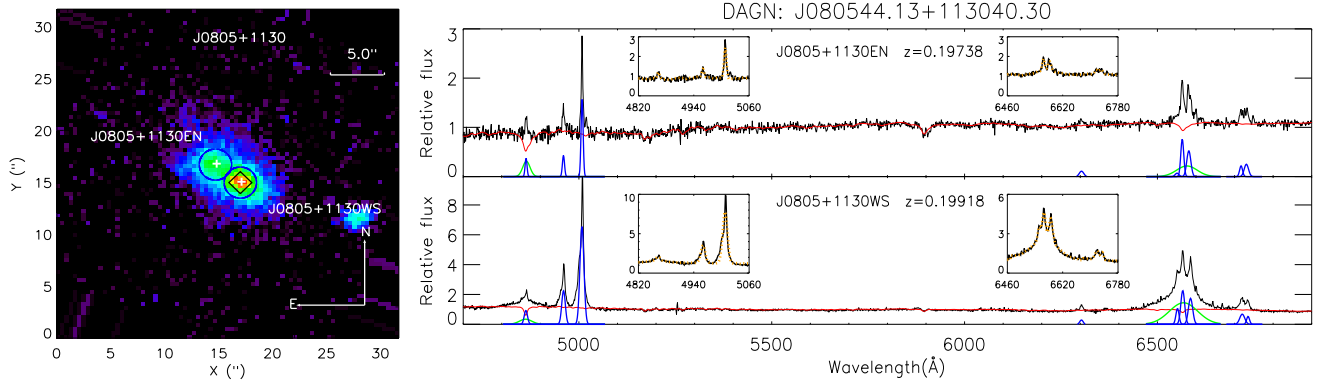


Figure A1. Same as Fig. 1 but for dual AGN J080544.13+113040.30.

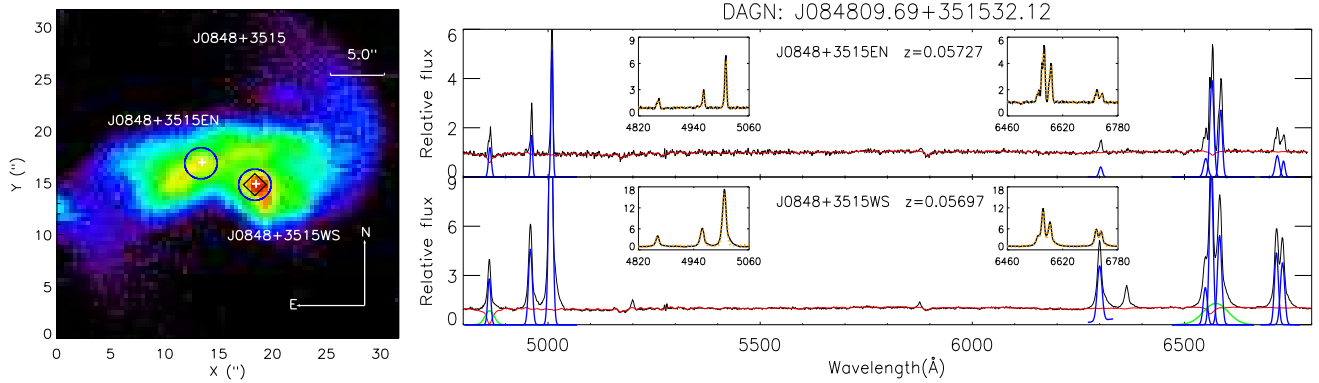


Figure A2. Same as Fig. 1 but for dual AGN J084809.69+351532.12.

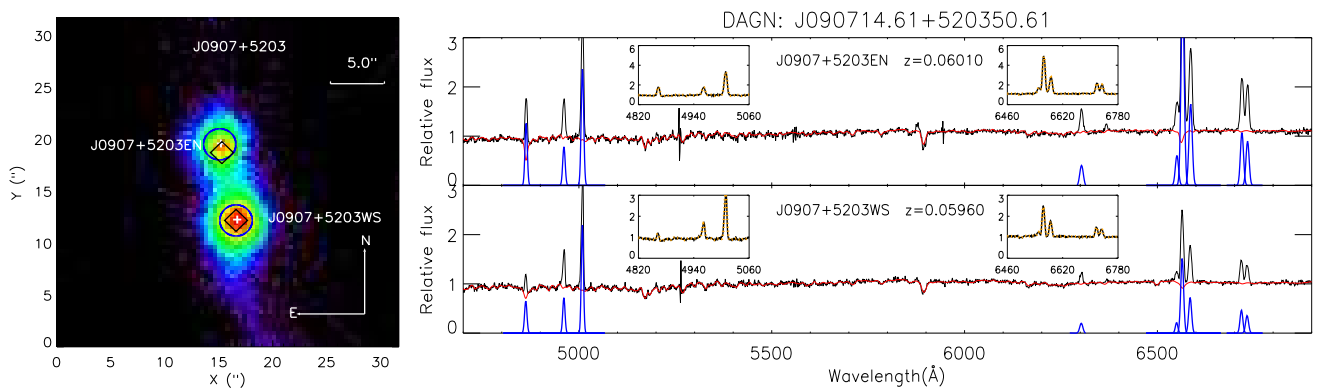


Figure A3. Same as Fig. 1 but for dual AGN J090714.61+520350.61.

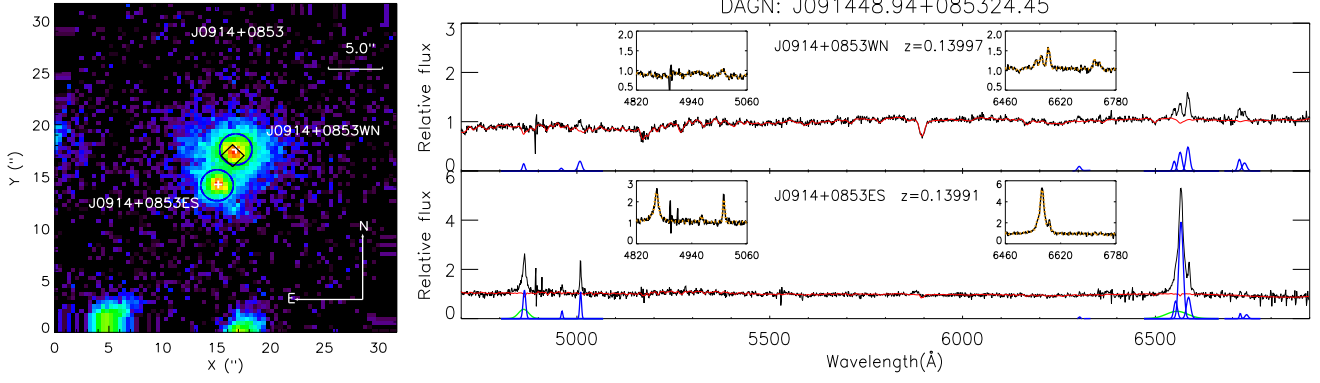


Figure A4. Same as Fig. 1 but for dual AGN J091449.05+085321.10.

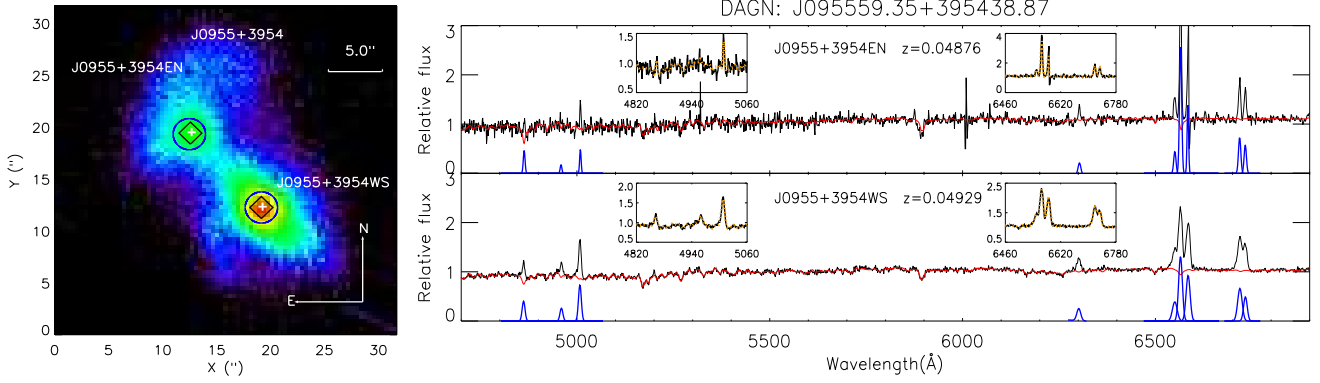


Figure A5. Same as Fig. 1 but for dual AGN J095559.35+395438.87.

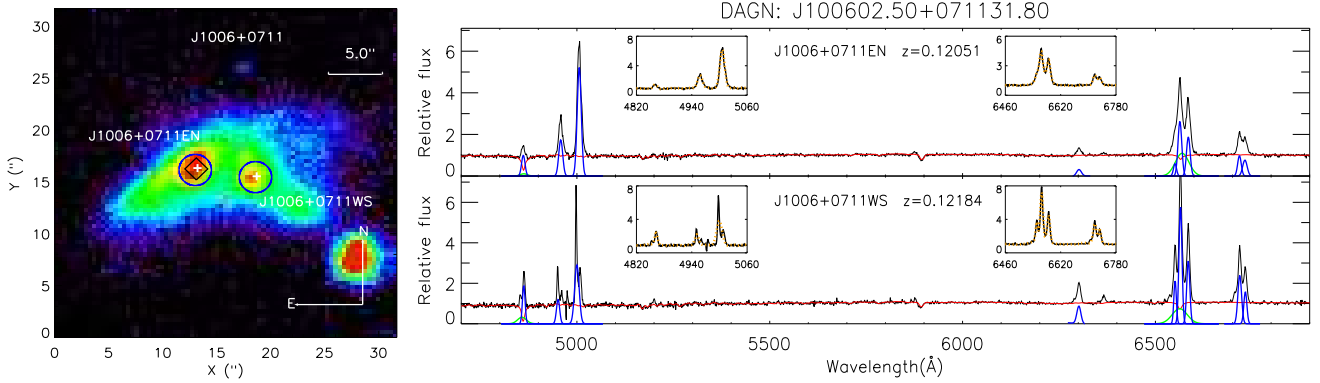


Figure A6. Same as Fig. 1 but for dual AGN J100602.50+071131.80.

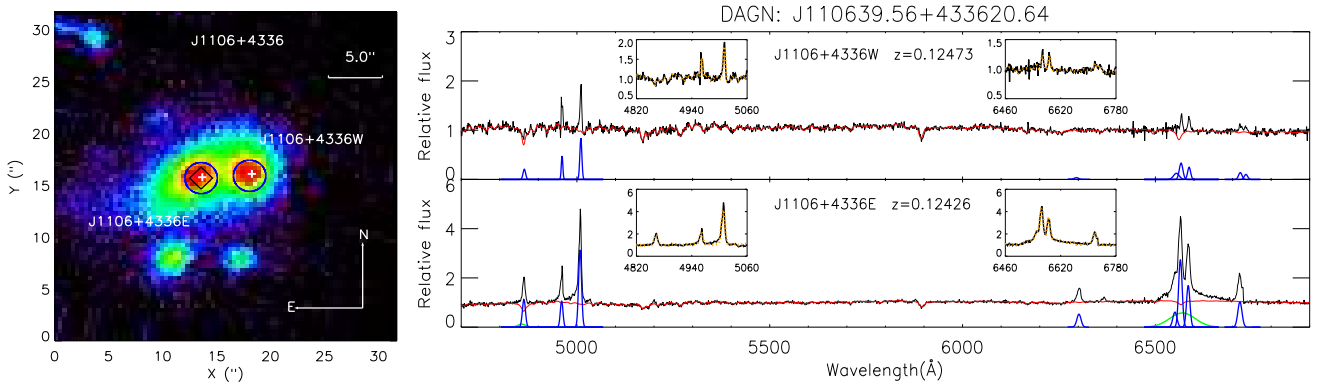


Figure A7. Same as Fig. 1 but for dual AGN J110639.56+433620.64.

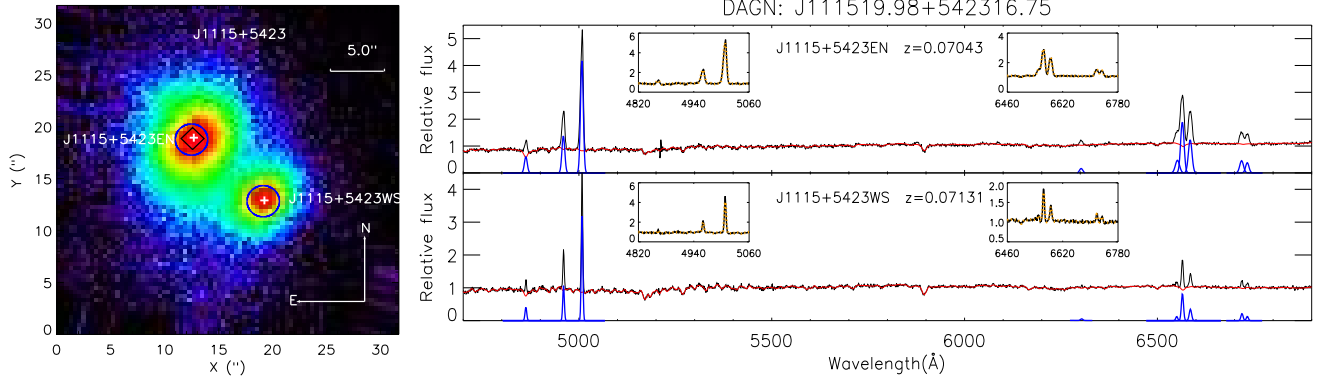


Figure A8. Same as Fig. 1 but for dual AGN J111519.98+542316.75.

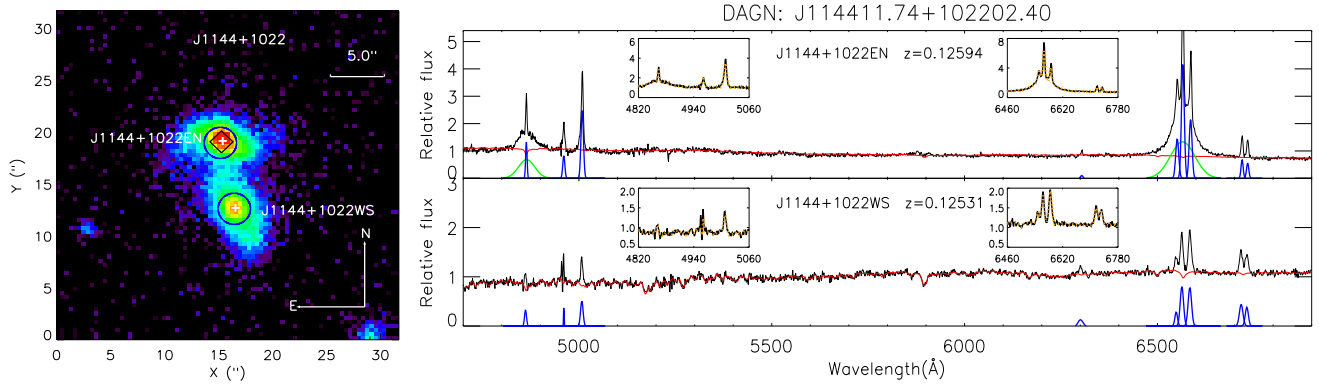


Figure A9. Same as Fig. 1 but for dual AGN J114411.74+102202.40.

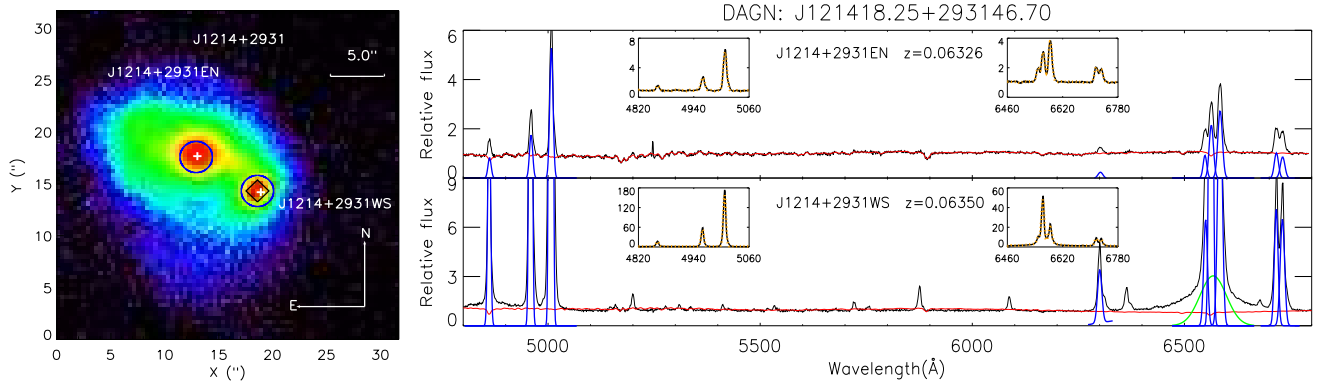


Figure A10. Same as Fig. 1 but for dual AGN J121418.25+293146.70.

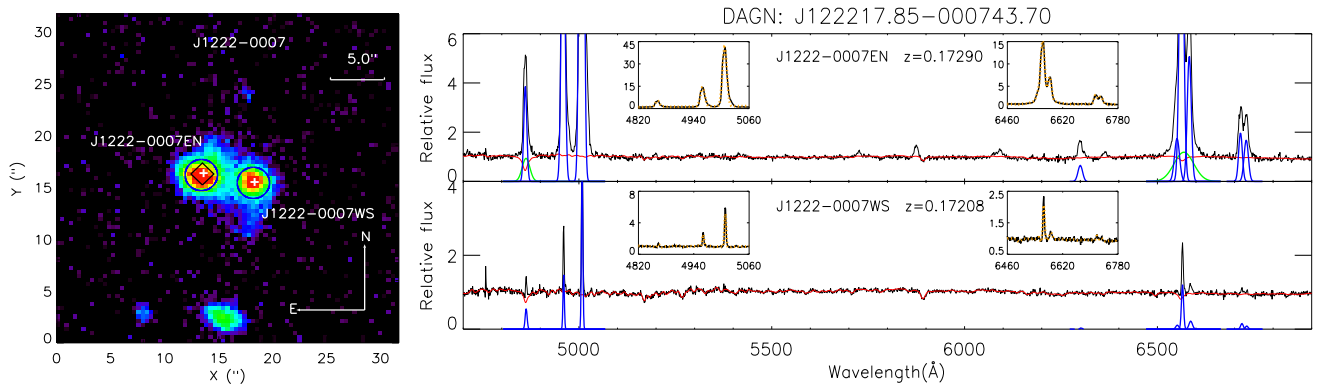


Figure A11. Same as Fig. 1 but for dual AGN J122217.85-000743.70.

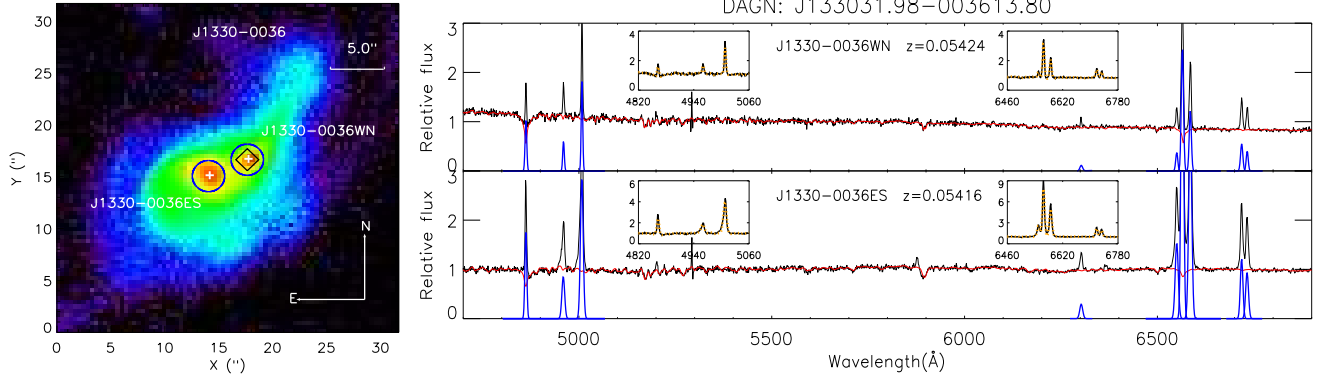


Figure A12. Same as Fig. 1 but for dual AGN J133031.98-003613.80.

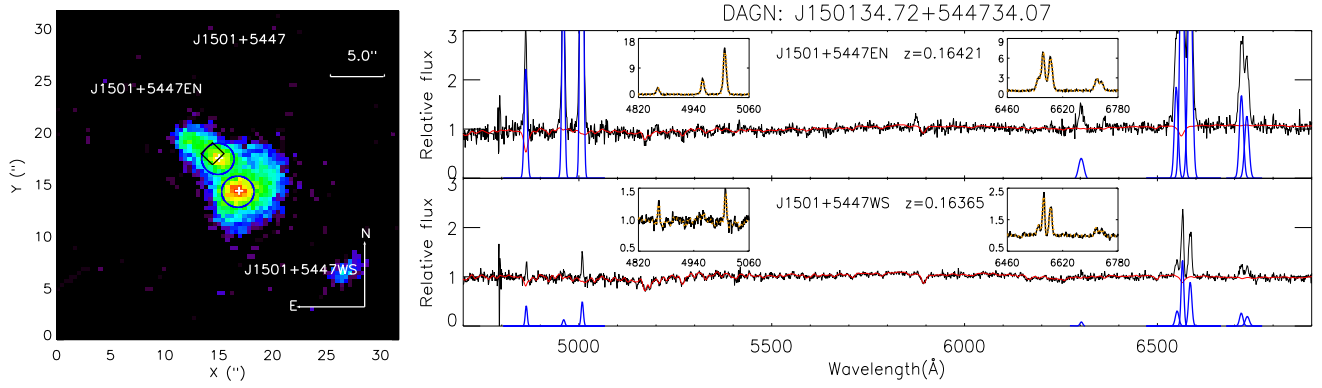


Figure A13. Same as Fig. 1 but for dual AGN J150134.72+544734.07.

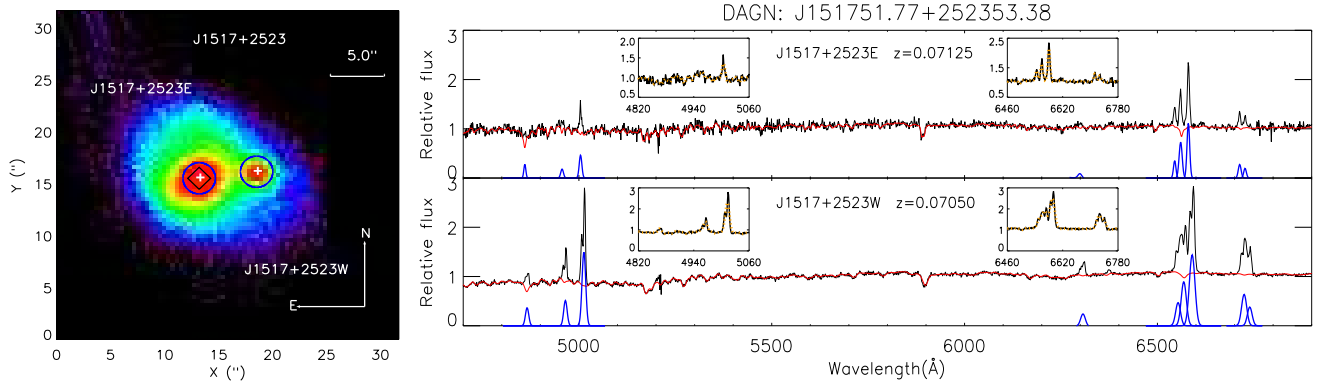


Figure A14. Same as Fig. 1 but for dual AGN J151751.77+252353.38.

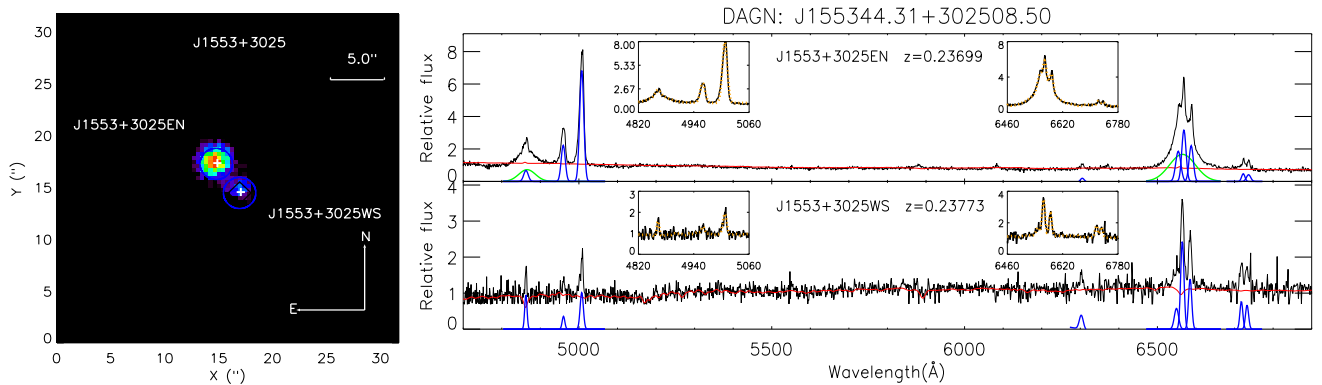


Figure A15. Same as Fig. 1 but for dual AGN J155344.31+302508.50.

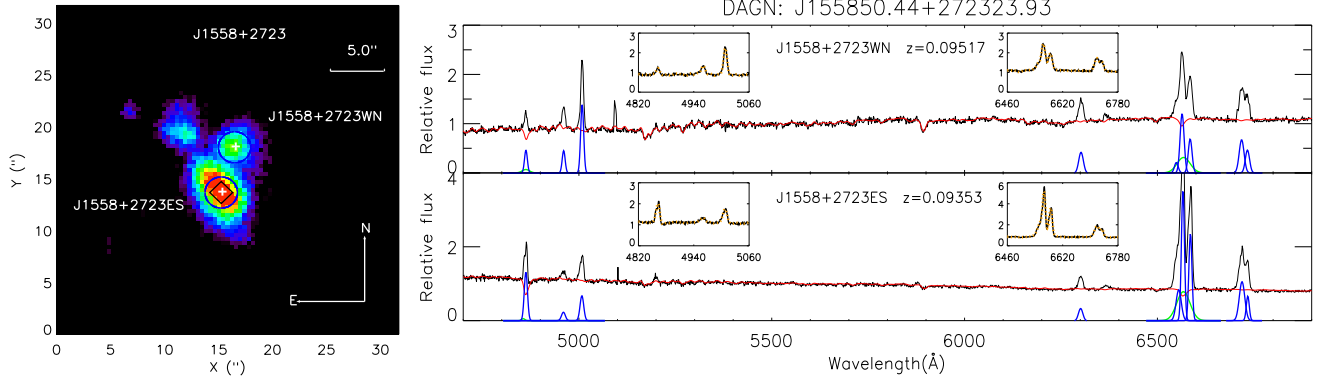


Figure A16. Same as Fig. 1 but for dual AGN J155850.44+272323.93.

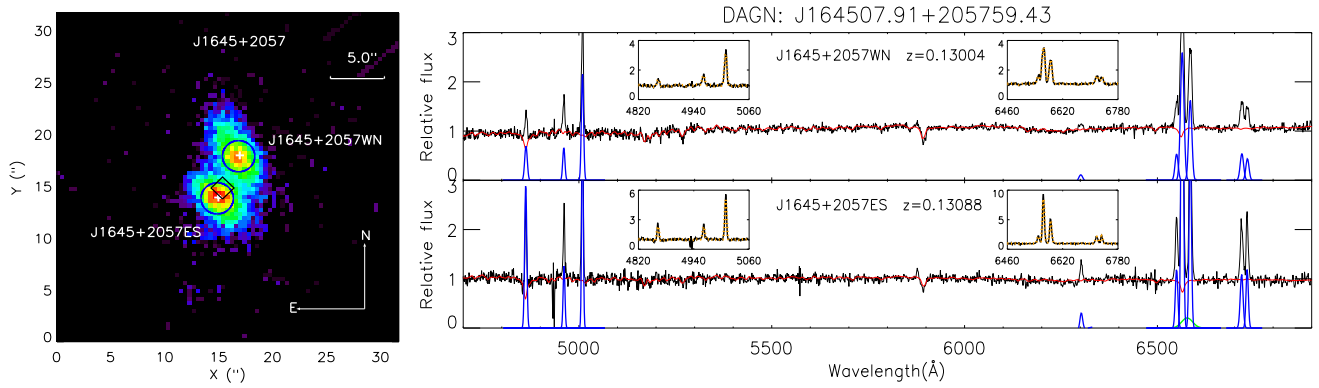


Figure A17. Same as Fig. 1 but for dual AGN J164507.91+205759.43.

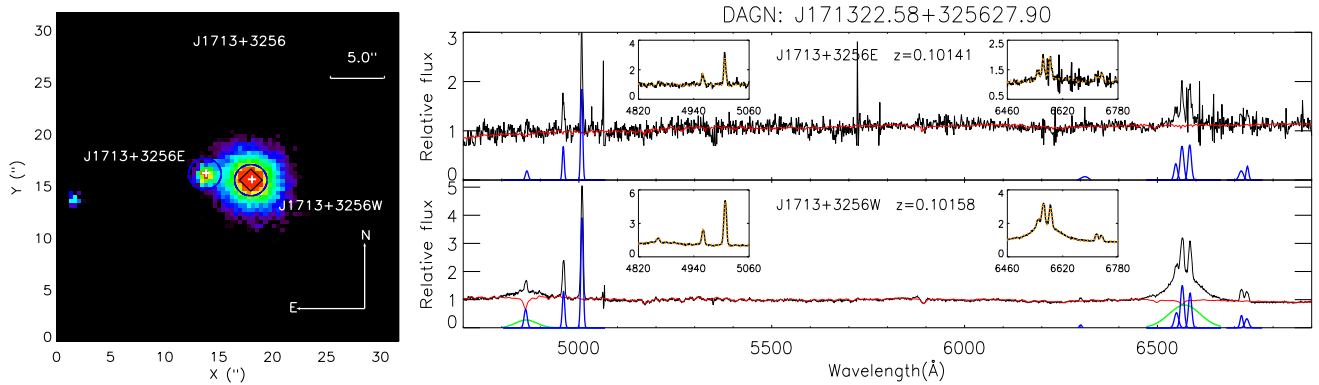


Figure A18. Same as Fig. 1 but for dual AGN J171322.58+325627.90.

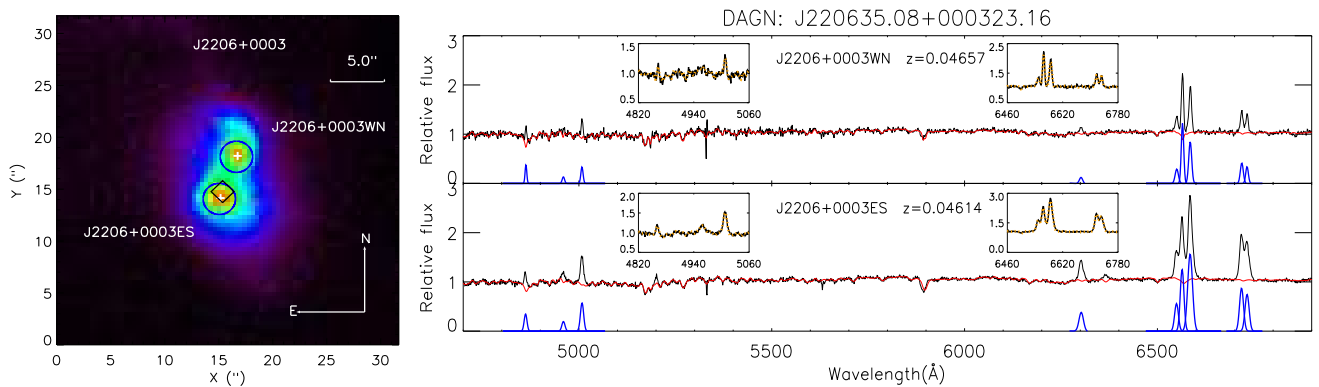


Figure A19. Same as Fig. 1 but for dual AGN J220635.08+000323.16.